



Structural Properties, Conductivity, Dielectric Studies and Modulus Formulation of Ni Modified ZnO Nanoparticles

Research Article

Sarita Sharma¹, Kirti Nanda¹, R.S. Kundu¹, R. Punia^{1,2,*} and N. Kishore¹

¹Guru Jambheshwar University of Science and Technology, Hisar 125001, Haryana, India

²Department of Physics, Indira Gandhi University, Meerpur, Rewari 123401, Haryana, India

*Corresponding author: rajeshpoonias13@gmail.com

Abstract. In the present manuscript, we have reported the structural, ac conductivity, dielectric studies and modulus formulation of $\text{Zn}_{1-x}\text{Ni}_x\text{O}$ ($x = 0.00, 0.10, 0.20, 0.30$) nanoparticles synthesized by sol-gel technique. The Rietveld refinement of X-ray powder diffraction data reveals that the samples possess hexagonal structure (space group - P63mc) of ZnO. The low intensity diffraction peaks corresponding to NiO comes into existence, it is suggested that phase segregation has occurred in the Ni doped ZnO nanoparticles. Average crystallite size has been estimated from XRD patterns, which is found to increase with increase in Ni content. AC conductivity and dielectric properties of Ni doped ZnO nanoparticles have been studied as a function of frequency (100 Hz to 10 MHz) of the applied ac signal in the temperature range of 323 K to 463 K. The results showed that ac conductivity increases while other parameters such as the real dielectric constant ϵ' and dielectric loss $\tan\delta$ decreases with frequency of applied field. The values of parameters ϵ' , $\tan\delta$ and ac conductivity are found to increase with increase temperature. In all the samples small polaron conduction mechanism is predominant. The variation of ϵ' , $\tan\delta$ and ac conductivity is observed to increase with increase in Ni dopant concentration in ZnO. The results of electrical modulus to study the relaxation dynamics of charge carriers indicate the presence of non-Debye type of relaxation in present samples.

Keywords. Sol-gel technique; Rietveld refinement; AC conductivity; Dielectric studies

PACS. 74.25.fc; 42.50.Wk

Received: March 18, 2015

Accepted: June 29, 2015

1. Introduction

Semiconducting nanomaterials have attracted great scientific attention due to their unique properties for different nanotechnological potential applications. ZnO, a II-VI semiconductor has attracted much attention because of its unique properties such as wide band gap (3.37 eV), large excitation binding energy (60 meV), near UV-emission, high transparency in the visible spectral range, low electrical resistivity, resistant to high temperature electronic degradation, etc. [1–4]. It is used in various devices such as ultra violet optoelectronic devices, high power and high frequency electronic devices, piezoelectronic transducers, chemical gas sensors, surface acoustic wave devices, antibacterial treatment, photocatalyst and additives in many industrial products [5–7]. ZnO doped with *transition metals* (TM) such as Mn, Fe, Ni, Co, V and Cr form dilute magnetic semiconductors, which are technically important due to their potential applications in spintronics [8]. The physical properties of ZnO such as electrical properties, piezoelectricity and structural defects can be tailored to specific use by doping different amounts of dopants in ZnO. There are many reports in literature several papers on the structural, optical, electrical and magnetic properties of Cu [9], V [10], Mn [11], Co [12] and Ni [13] doped ZnO nanomaterials. But the dielectric behavior of ZnO based nanoparticles is less explored as compared to its other properties.

Different chemical methods as chemical precipitation [14], sol-gel synthesis [15], and hydrothermal reactions [16] have been developed for the preparation of ZnO based nanomaterials. Sol-gel method is one of the most important wet chemical methods for the preparation of metal oxide nanoparticles which is based on the hydrolysis of reactive metal precursors. In the present work, Ni modified ZnO nanoparticles have been synthesized by sol-gel method and structural, ac conductivity and dielectric studies of Ni- modified ZnO nanoparticles are reported.

2. Experimental Detail

2.1 Synthesis

The various compositions of the system $\text{Zn}_{1-x}\text{Ni}_x\text{O}$ ($x = 0.0, 0.1, 0.2, 0.3$) were prepared as polycrystalline nanoparticles powders by sol-gel technique. The zinc acetate ($\text{Zn}(\text{CH}_3\text{COO})_2 \cdot 2\text{H}_2\text{O}$) and nickel acetate ($\text{Ni}(\text{CH}_3\text{COO})_2 \cdot 4\text{H}_2\text{O}$) of *analar* (AR) grade were dissolved in distilled water in proper stoichiometric ratio separately and the resulting solutions were mixed and stirred to ensure homogenous mixing. Then volume of monoethanolamine was added slowly. The final solution was heated at 60-70 °C for one hour with continuous stirring using magnetic stirrer to convert sol into gel form. The gel was cooled at room temperature for 2-3 hours and the precipitates were filtered and washed with distilled water, ethanol and acetone subsequently to remove impurities. The precipitates were dried at 200 °C in an electric muffle furnace for one hour and subsequently grinded in mortar and pestle to make fine powder. The calcination of all samples was performed at 700 °C in electric muffle furnace for 3 hours each.

2.2 Characterization

Structural analysis of the samples were performed by using Rigaku Table-Top X-ray diffractometer with CuK_α radiation ($\lambda = 1.54\text{\AA}$) at 40KV and 100 mA with scanning rate of 2 degree per minute. The Rietveld refinement was performed using FULLPROF Program. Calcined powder samples were pressed under a load of 50 tons for 2 minutes into disc shaped pellets with diameter 11 mm and thickness 1 mm. Pellets were coated with silver paste forming parallel plate capacitor. Conductivity measurements were carried out by using Alpha-A High Resolution Dielectric, Conductivity, Impedance, and Gain Phase Modular Measurement System by Novo control Technologies GmbH & Co. KG in frequency range of 100 Hz to 10 MHz and temperature ranging from 323 K to 463 K.

3. Results and Discussion

3.1 Structural Analysis

3.1.1 XRD Analysis

The X-ray diffraction patterns of unmodified and nickel modified ZnO samples annealed at 700 °C are shown in Figure 1. The average crystallite size has been calculated from the *full width at half maxima* (FWHM) of the diffraction peaks using the Debye-Scherrer equation [13]

$$D = k\lambda/(\beta \cos\theta) \quad (3.1)$$

where D is average crystalline size, k is shape factor, λ is wavelength of X-ray radiation, β is FWHM and θ is the Bragg's angle. The most intense peak (101) in the XRD pattern has been used to calculate the average crystalline size and it is listed in Table 1. Perusal of data presented in Table 1 shows that the average crystalline size increases with increase in Ni doping. The similar behavior of increase in average crystalline size with Ni doping has also been observed by other researcher [17].

3.1.2 Rietveld Analysis

The phase analysis has been carried out by comparing the XRD data with the standard JCPDS database, and the data was refined by Rietveld refinement technique using FULLPROF Program (Rodriguez-Carvajal J, 2000). In the present study, the simulated XRD patterns for the Rietveld analysis are generated with the following phases: (ZnNi)O (hexagonal, space group - P63mc), and NiO (cubic, space group - Fm-3m) phases. Rietveld refinement is used to minimize $\sum w_i(y_i(\text{obs}) - y_i(\text{calc}))^2$, where $y_i(\text{obs})$, $y_i(\text{calc})$ are observed and calculated powder diffraction intensities for the i th point, respectively and weight $w_i = 1/y_i(\text{obs})$. Weighted (R_{wp}) and unweighted (R_p) profile R-factors are defined as [18]

$$R_{wp} = \frac{[\sum w_i(y_i(\text{obs}) - y_i(\text{calc}))^2]^{\frac{1}{2}}}{\sum w_i((y_i(\text{obs}))^2)} \quad (3.2)$$

The structure factor (R_F) and Bragg R-factor (R_B) are defined as [19]

$$R_p = \frac{\sum |y_i(\text{obs}) - y_i(\text{calc})|}{\sum y_i(\text{obs})} \quad (3.3)$$

$$R_F = \frac{\sum |(I_k(\text{obs}))^{\frac{1}{2}} - (I_k(\text{calc}))^{\frac{1}{2}}|}{\sum (I_k(\text{obs}))^{\frac{1}{2}}}, \quad (3.4)$$

$$R_B = \frac{\sum |(I_k(\text{obs}) - (I_k(\text{calc})))|}{\sum I_k(\text{obs})} \quad (3.5)$$

where I_k is the integrated intensity of the k th reflection. The expected R -factor (R_{exp}) (statistically best possible value for R_{wp}) is defined as [20]

$$R_{\text{exp}} = \left[\frac{N - P}{\sum w_i (y_i(\text{obs}))^2} \right]^{\frac{1}{2}} \quad (3.6)$$

where N is the total number of points, P is the number of refined parameters. Goodness-of-fitting (GOF) and Chi square (χ^2) are defined as [21]

$$GOF = \frac{R_{wp}}{R_{\text{exp}}}, \quad (3.7)$$

$$\chi^2 = \left(\frac{R_{wp}}{R_{\text{exp}}} \right)^2. \quad (3.8)$$

The rietveld refined XRD plot and the residual of fitting are plotted for various Ni modified ZnO nanoparticles (calcined at 700 °C) in Figure 1. For prepared samples, the value of χ^2 is less than six, suggests the good structural refinement of the studied nanoparticles. The refined structural parameters: occupancy (N), R -factors such as R_F , R_B , R_p , R_{exp} , R_{wp} , GOF and χ^2 obtained after refinement are given in Table 2 to 4. From this data, it has been concluded that all the samples have hexagonal wurtzite structure. An additional diffraction peaks corresponding to NiO comes into existence in Ni modified ZnO nanoparticles. It suggests that phase segregation has occurred in the Ni modified ZnO nanoparticles. The intensity of NiO peaks increased sharply with increasing nickel concentration [22].

Since, the ionic radius of Ni^{2+} (0.55 Å) is less than that of Zn^{2+} (0.60 Å) consequently, there is slight variation in lattice parameters of modified ZnO nanoparticles. This causes a small shift of all the peaks to the lower angles. It gives the indication for substitution of Nickel in the ZnO crystalline structure. With Ni doping in ZnO, the more Ni ions get substituted on the surface i.e., along c -axis upto $x = 0.2$. Due to the presence of Ni ions at surface, interparticle attraction increases that accelerates the growth of nucleation, so there is increase in lattice parameter as one goes from $x = 0.0$ to 0.2. When the Ni content further increases ($x = 0.2$) excess Ni would substitute along a -axis and/or b -axis. This causes the reduction in lattice parameter as shown in Table 2. It is due to the intraparticle contribution, arising from different coordination of ions [15].

3.2 AC Conductivity

The ac conductivity $\sigma'(\omega)$ was derived from the complex data using the relation

$$\sigma'(\omega) = \omega \epsilon_0 \epsilon' \tan \delta$$

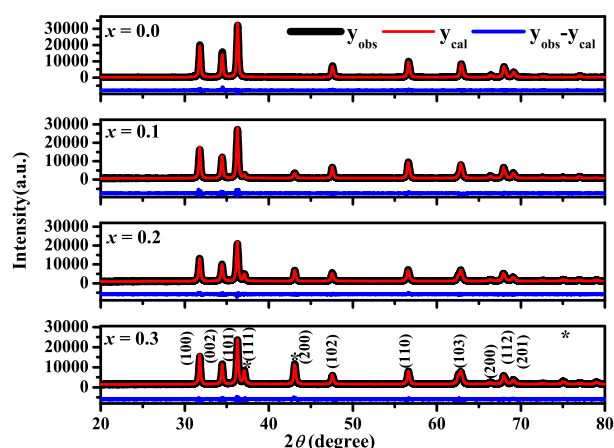


Figure 1. Rietveld refinement plot of various compositions of $\text{Zn}_{1-x}\text{Ni}_x\text{O}$ powder samples calcined at 700°C .

where ω is angular frequency, ϵ_0 is the permittivity of free space, ϵ' is real part of dielectric constant and $\tan\delta$ is dielectric loss. The frequency dependent conductivity $\sigma'(\omega)$ has been observed for pellet samples with $(0.0 \leq x \leq 0.3)$ in temperature range of $323\text{K} \leq T \leq 463\text{K}$. The conductivity-frequency spectra as shown in Figure 2 for $\text{Zn}_{0.7}\text{Ni}_{0.3}\text{O}$ sample show two distinct frequency dependent dispersion regions (region II and III). In region I, the conductance is approximately equal to dc value (σ_{dc}). For dispersive regions (II and III) cross over frequency increases with increase in temperature as shown by solid lines in Figure 2 [23,24]. With increase in frequency, the conductivity spectra become more dispersive. The frequency conductivity spectra exhibit multiple step-like increments which is a characteristic of a potential profile with multiple activation energies [25].

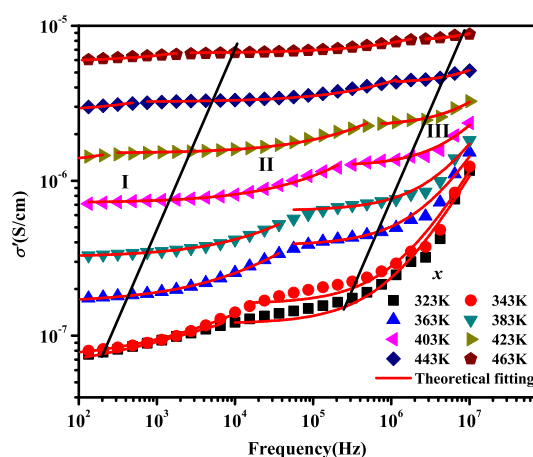


Figure 2. Measured total ac conductivity (σ') for $\text{Zn}_{0.7}\text{Ni}_{0.3}\text{O}$ composition, shown as function of frequency at eight different temperatures. The solid lines in the figure are the best fits obtained from fitting of experimental data with Jonscher's power law.

Generally ac conductivity behavior is analyzed using the Jonscher's power law [26],

$$\sigma'(\omega) = \sigma_{dc} \left[1 + \left(\frac{\omega}{\omega_H} \right)^n \right] \quad (3.9)$$

where σ_{dc} is dc conductivity, ω_H is crossover frequency separating dc regime (plateau region) from the dispersive conduction and n is frequency exponent that lies between 0 and 1. Equation (3.9) describes the conduction mechanism with the first term in RHS is the dc conductivity due to band conduction and the second term shows the transport properties of polarons, ions and electrons [27]. The ac conductivity cannot be accounted by Equation (3.9), rather two such formulae have been used in different frequency regions to explain the presence of two relaxation mechanisms [28]. The conductivity at low frequencies have almost a constant value assigned to dc conductivity for grain boundaries (σ_{gb}) and the frequency independent plateau in region II is to the dc conductivity for grains (σ_g). The values of σ_{dc} , ω_H and n are obtained by the fitting of the frequency dependent conductivity ($\sigma'(\omega)$) data measured experimentally at different temperatures with Equation (3.9) for different frequency regions. Figure 2 shows the experimental data fitted with Jonscher's universal power law (Equation (3.9)) in different frequency regions for $Zn_{0.7}Ni_{0.3}O$ sample.

The value of n for different frequency regions increases with the increase in temperature. Figure 3 illustrates the variation of exponent n with temperature at different compositions for high frequency dispersion region. As n increases with increasing temperature in all studied samples, then the conduction process can be explained with the small polaron quantum mechanical tunneling theory. If small polarons are formed, then according to tunneling model [27] frequency exponent (n) becomes

$$n = 1 - \frac{4}{\ln\left(\frac{1}{\omega\tau_0}\right) - \frac{\omega_H}{K_B T}} \quad (3.10)$$

Equation (3.10) suggests that n increases with increase in temperature. In present samples small polaron conduction mechanism is predominant. Equation (3.9) shows that conductivity increases with the increase of frequency which is in good agreement with our results. This behavior can be explained on the basis that charge carriers are transferred between different localized states and trapped charges are liberated with the help of pumping force of the applied frequency [29]. The electron-hopping model explains the electrical conduction mechanism in which electron hopping between the lattice sites takes place. Consequently, the hopping frequency of charge carriers increases with the increase in frequency resulting in an increase in conductivity. Electrical conductivity increases with the increase in temperature due to the increase in drift mobility of the thermally activated charge carriers [30].

The inverse temperature variation of dc conductivity for grain boundaries and grains follows the Arrhenius equation [31]

$$\sigma_{dc}(T) = \sigma_0 \exp[-(E_A/kT)] \quad (3.11)$$

where σ_0 is a pre-exponential parameter that depends on semiconductor nature, E_A denotes the thermal activation energy of electrical conduction, and k is Boltzmann's constant. The values

of activation energies for grain boundaries (E_{gb}) and grains (E_g) are presented in Table 1 for all samples. Persual of data presented in Table 1 indicates that activation energy of grain boundaries and grains decreases with increase in Ni doping concentration in ZnO, suggesting thereby the increase in conductivity [32]. These grain boundaries act as insulating layer between grains thus creating the interfacial/space polarization. The data tabulated in Table 1 at (10^3Hz , 423 K) shows that conductivity increases with the increase in Ni concentration. Several factors influence the conductivity such as Ni^{2+} ion concentration, crystal structure perfection, homogeneity of microstructure and grain size. Generally, conductivity of polycrystalline materials increases with the increase in grain size. Larger grains imply a small number of insulating grain boundaries, which act as a barrier to the flow of electrons. Larger grains imply larger grain to grain surface contact area and therefore, electron flow increases [33]. The grain size (calculated from XRD data) of Ni modified ZnO nanoparticles increases with increase in Ni concentration and hence conductivity increases as the grain size increases. The higher value of conductivity for the sample with $x = 0.3$ may be due to the surface charge polarization owing to large surface area of individual grains and the presence of localized state in the forbidden energy gap which arises due to lattice imperfections [33].

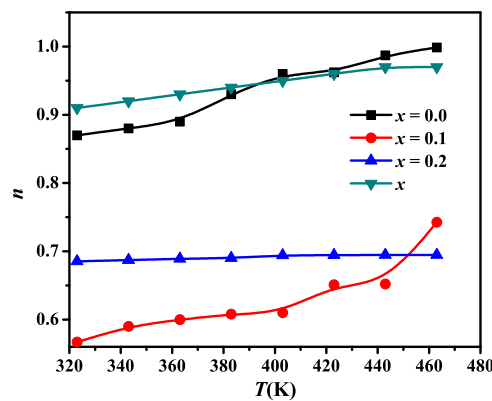


Figure 3. Plot of frequency exponent n with temperature at different compositions for high frequency dispersion region.

3.3 Dielectric Studies

3.3.1 Dielectric Constant

The dielectric properties of materials are characterized by the complex dielectric constant (ϵ) which is represented by:

$$\epsilon = \epsilon' - j\epsilon'', \quad \text{where } j = \sqrt{-1}. \quad (3.12)$$

The real part (ϵ') of dielectric constant is the measure of the amount of energy stored in a dielectric due to the applied field and the imaginary part (ϵ'') of dielectric constant describes the dissipated energy in dielectric. The value of real part of dielectric constant (ϵ') is calculated

using relation

$$\epsilon' = Ct/A\epsilon_0 \quad (3.13)$$

where ϵ_0 is the permittivity of free space, t is the thickness of pellet, A is the cross sectional area and C is the capacitance of pellet. The imaginary part of dielectric constant (ϵ'') of samples is calculated using the relation

$$\epsilon'' = \epsilon' \tan \delta \quad (3.14)$$

where $\tan \delta$ is the dielectric loss. The real part (ϵ') of dielectric constant decreases with increase in frequency for all studied samples. Figure 4 shows the variation of ϵ' with frequency for sample with $x = 0.3$ at different temperatures. It is observed that all samples exhibit the dielectric dispersion and the value of ϵ' decrease with the increase in frequency. The decrease in dielectric constant is rapid at low frequency and becomes slow at higher frequencies, approaching to frequency independent behavior. The observed frequency dependent dielectric behavior which can be explained by Maxwell-Wagner type relaxation [34]. According to this model, the material with inhomogeneous structure consists of well conducting grains which are separated by insulating grain boundaries. When the external electric field is applied, the charge carriers can easily migrate into the grains and accumulated on the grain boundaries. So, large polarization and high value of dielectric constant is produced in this process. The high values of dielectric constant at low frequencies may be due to the interfacial dislocations, oxygen vacancies, charged defects, grain boundaries effect and interfacial/space charge polarization due to heterogeneous dielectric structure. The grain structure and porosity causes inhomogeneity in the system. The decrease in dielectric constant with frequency because of the fact that polarizability of species decreases with increase in frequency and then reaches a constant value which is attributed due to the fact that beyond a certain frequency of applied external electric field the hopping between different transition metal ions cannot follow the external field [34]. The polarizability of metal ions is found to lag behind the applied external electric field as the frequency is increased.

Persual of data shown in Figure 4(inset) represent the variation of ϵ' with temperature at different frequencies for $x = 0.3$ sample. The similar variation is observed for all other studied samples. The values of ϵ' increase with increase in temperature indicating thereby the semiconducting nature of Ni modified ZnO. The dielectric dispersion of dielectric constant is weak in low temperature region. With increase in temperature, the dielectric constant increases sharply in low frequency region and in high frequency region it increases slowly. This can be explained on the basis that charge carriers cannot possess strong contribution to polarization and dielectric behavior because charge carriers cannot orient themselves in the direction of applied external electric field at low temperature. The bound charge carriers get enough thermal excitation energy to be able to obey the change in the external field with the increase in temperature. The disorder in lattice causes thermal excitations of atoms about their lattice points. The contribution of space charge towards polarization may be attributed to the purity of the crystal. This in return enhances their contribution to the polarization leads to an increase in dielectric behavior.

The compositional dependence of real part of dielectric constant ϵ' for $\text{Zn}_{1-x}\text{Ni}_x\text{O}$ ($x = 0.0, 0.1, 0.2, 0.3$) at (10^6 Hz, 323 K) presented in Table 1. It is observed that dielectric constant increases with increase in Ni concentration in ZnO matrix. Dielectric constant increases with the increase in size of nanoparticles. Similar variation of ϵ' with average crystalline size is observed by other researchers [35]. This phenomenon is based on space charge polarization and reversal of direction of polarization. It can be explained on the basis of the fact that polarization is a size dependent property (polarization is more for larger average crystalline size). From XRD data it is observed that average crystalline size (D) increases with the increase in Ni concentration in ZnO. With the increase in D the volume of crystals (V_p) increases and consequently volume of interfaces (V_i) decreases. The contribution of electronic relaxation polarization to ϵ' inside the particles increases due to increases of (V_p). At interfaces contribution to ϵ' by space charge polarization and rotation of the direction of polarization diminishes because of the decrease in the value of (V_i). As a result ϵ' increases as average crystalline size of samples increases [36].

3.3.2 Dielectric Loss

The dielectric loss factor $\tan\delta$, represents the energy dissipation in dielectric system and it arises when the polarization lags behind the applied electric field. The variation of $\tan\delta$ with frequency at different temperatures for $x = 0.1$ sample is shown in Figure 5. Figure 5(inset) shows the temperature dependence of $\tan\delta$ at selected frequencies for $x = 0.1$ sample. All other samples show qualitatively similar type of variations for $\tan\delta$. The dielectric loss $\tan\delta$ decreases rapidly in low and mid frequency region. In high frequency region it becomes almost frequency independent since domain wall motion is inhibited and magnetization is forced to change rotation. It is observed from the spectra that dielectric loss is high at higher temperatures and lower frequencies. It can be explained on the basis that at lower frequencies the trend in loss is due to space charge polarization and at higher temperature behavior of loss may be due to macroscopic distribution of charges [37]. Further, it can be explained by Shockley-Read mechanism. According to this mechanism, at lower and middle frequencies and at higher temperatures the impurity ions in the bulk crystal matrices capture the surface electron, causing the surface charge polarization at the surfaces. This process increases with increase in temperature.

The appearance of peak in dielectric spectra at all temperatures is shown in Figure 5 for sample with $x = 0.1$. This peak shifts towards higher frequency with rise in temperature due to increase in hopping frequency of charge carriers between metal ions [38]. However, low value of $\tan\delta$ at higher frequencies shows the ability of these materials to be used in high frequency devices. The dielectric loss increases with increase in doping of Ni in ZnO as presented in Table 1 at (10^3 Hz, 343 K). It can be explained on the basis that polarization is the size dependent property (for larger average crystalline size particle polarization will be more). So, dielectric loss increases with increase in Ni ion concentration in ZnO [36].

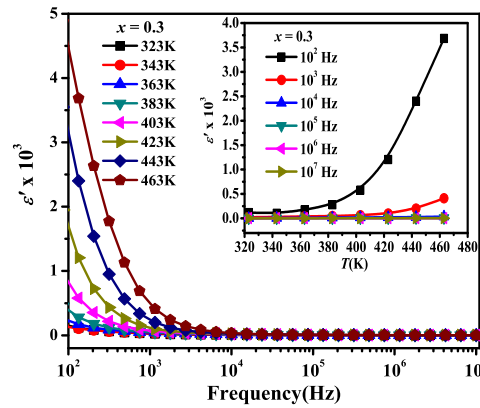


Figure 4. Frequency dependence of real part of dielectric constant (ϵ') for $x = 0.3$ sample at different temperatures (Inset: Temperature dependence of real part of dielectric constant (ϵ') at various frequencies for $\text{Zn}_{1-x}\text{Ni}_x\text{O}$ ($x = 0.3$)).

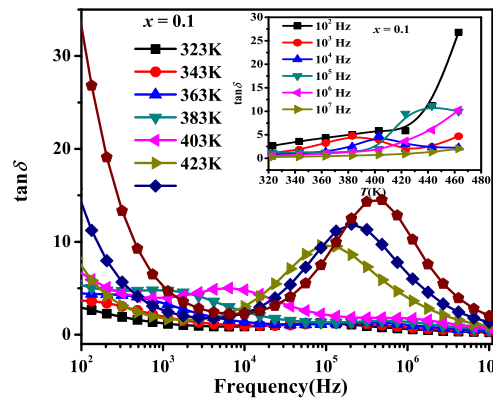


Figure 5. Frequency dependence of dielectric loss ($\tan \delta$) at various temperatures for $\text{Zn}_{1-x}\text{Ni}_x\text{O}$ ($x = 0.1$) (Inset: Temperature dependence of loss ($\tan \delta$) at various frequencies for $\text{Zn}_{1-x}\text{Ni}_x\text{O}$ ($x = 0.1$)).

3.4 Electric Modulus Formulation

In the modulus formalism, the electrical relaxation is appropriately represented by the electric modulus as [39]

$$M^*(\omega) = M' + jM'' = \frac{1}{\epsilon_\infty} \left[1 - \int_0^\infty e^{-j\omega t} \left(\frac{-d\phi}{dt} \right) dt \right] \quad (3.15)$$

where ϵ_∞ is high frequency asymptotic value of the real part of dielectric constant and $\phi(t)$ is the relaxation function and it follows a stretched exponential function called *Kohlrausch-Williams-Watts* (KWW) function [40] given by

$$\phi(t) = \exp \left[- \left(\frac{t}{\tau} \right)^\beta \right] \quad (3.16)$$

where τ is the conductivity relaxation time and the exponent “ β ” indicates the deviation from the Debye-type relaxation. The electric modulus data have been analyzed using the theoretical expression given in Equation (3.15). Typical features of $M^*(\omega)$ include a broad, asymmetric peak in the imaginary part and a sigmoidal step in the real part. Figure 6 shows the frequency dependence of real (M') and imaginary (M'') part of electric modulus at different temperatures with $x = 0.0$. All other samples show qualitatively similar type of variations for M' and M'' with frequency at different temperatures. It is observed from Figure 6 that at low frequencies, M' approaches zero at all the temperatures under study, suggests the suppression of the electrode polarization. M' reaches a maximum value corresponding to $M_\infty = 1/\epsilon_\infty$ due to the relaxation process. This increase in M' can be attributed to the conduction phenomena [41]. It is also observed that the value of M' decreases with the increase in temperature. The value of M'' indicates the energy loss under electric as shown in Figure 7.

The imaginary part of the electric modulus (M'') is defined [42] as

$$M'' = \frac{M''_{\max}}{(1 - \beta) + \frac{\beta}{1 + \beta} [\beta(\omega_{\max}/\omega) + (\omega_{\max}/\omega)^\beta]} \quad (3.17)$$

where M''_{\max} is the peak value of M'' and ω_{\max} is the corresponding frequency. The equation (3.17) is theoretical fitted to the experimental data for present samples. It is observed from Figure 7 that the experimental data are well fitted for $x = 0.3$ sample. The value of β is calculated from fitting of equation (3.17) and it is found to be temperature dependent. The plot of β versus temperature is depicted in Figure 8. β increases gradually with the increase in temperature, indicating that as the temperature increases, interactions between Ni^{2+} ions and surrounding matrix decreases. The parameter β increases with increase in Ni concentration, its values are presented in Table 1. In the present study, the value of $\beta < 1$ (Table 1) which suggests that the non-Debye type of relaxation prevails in these samples [43].

The characteristic frequency at which M'' is maximum (M''_{\max}), corresponds to relaxation frequency ($f_{M''}$) and is used for the evaluation of relaxation time $\tau_{M''} = 1/2\phi f_{M''}$. With rise in temperature M'' peak frequencies shift to higher values in indicates thermally activated relaxation process [44]. The relaxation frequency indicates the transition from long range to short range mobility. The reciprocal temperature dependence of $\tau_{M''}$ also satisfies the Arrhenius relation $\tau_{M''} = \tau_0 \exp[-(E_g(M'')/kT)]$. The activation energy for the conductivity relaxation time, $E_g(M'')$ has been calculated from the least square fitting of data as shown in Figure 9 and values are presented in Table 1. The M'' plots only give the activation energy for grains; there is no indication of the capacitance arising due to grain boundaries. It is observed from Table 1 that the value of activation energies for conductivity relaxation $E_g(M'')$ is similar to that of dc conduction (E_g) which suggests that the mechanism of electrical conduction and dielectric polarization is same in these samples. The normalized plots of the imaginary part of the electric modulus (M''), where the frequency axis is scaled by the peak frequency and M'' axis is scaled by M''_{\max} is shown in Figure 10. A perfect overlapping of all the curves on a single master curve is observed for all the temperatures. This suggests that the conduction mechanism is temperature independent for the present samples.

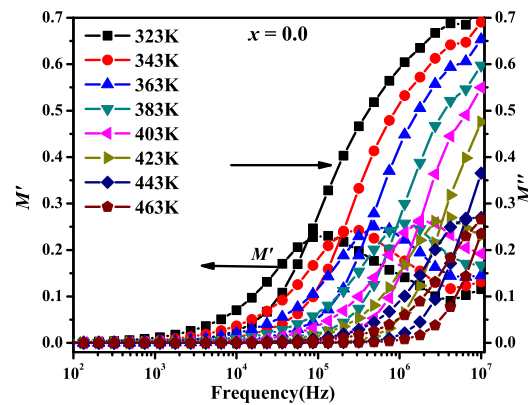


Figure 6. Frequency dependence of the real (M') and imaginary part (M'') of electric modulus for $x = 0.0$ at different temperatures.

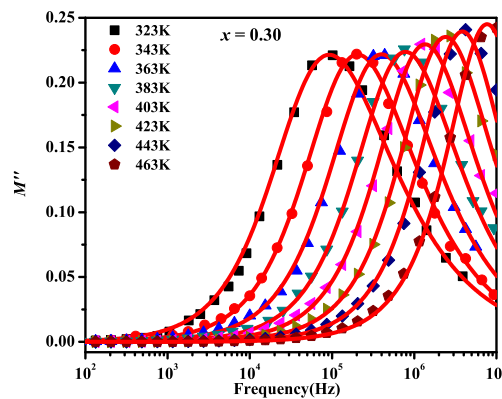


Figure 7. Imaginary part (M'') of the electric modulus as a function of frequency at different temperatures and solid lines are the fitted curves for $x = 0.3$.

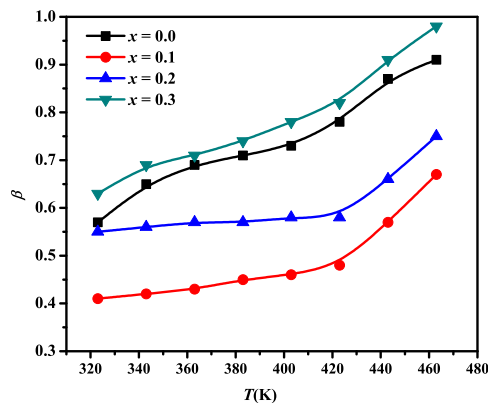


Figure 8. β versus T for various compositions of $\text{Zn}_{1-x}\text{Ni}_x\text{O}$ nanoparticles.

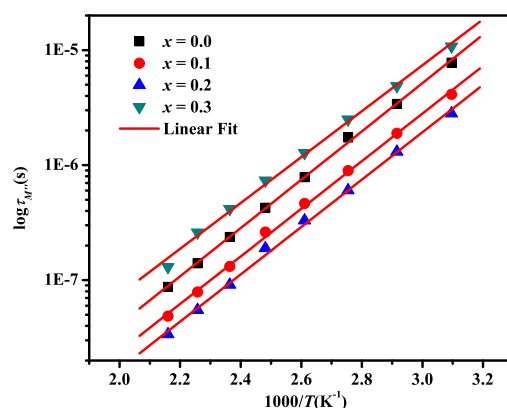


Figure 9. Arrhenius plot of relaxation times ($\tau_{M''}$) for various compositions of $\text{Zn}_{1-x}\text{Ni}_x\text{O}$ nanoparticles.

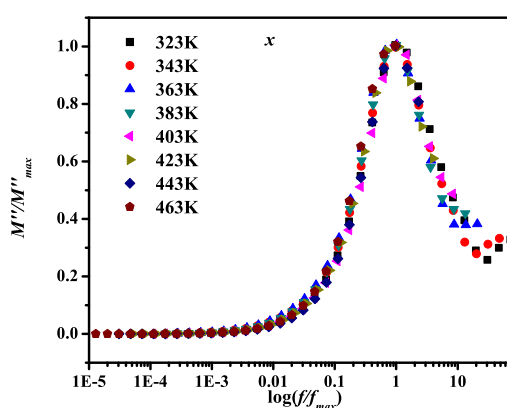


Figure 10. Normalized plots of dielectric modulus against normalized frequency for $x = 0.3$ at various temperatures.

Table 1. Compositional variation of average crystalline size (D), ac conductivity $\sigma'(\omega)$ at (10^3 Hz, 423 K), real part of dielectric constant (ϵ') at (10^6 Hz, 323 K), dielectric loss ($\tan\delta$) at (10^3 Hz, 343 K), activation energies (E_{gb} , E_g and $E_g(M'')$) and stretched exponent parameter (β).

Sample	$D(\text{nm})$	$\sigma'(\omega) \times 10^{-6}$ (S/cm)	ϵ'	$\tan\delta$	$E_{gb}(\text{eV})$	$E_g(\text{eV})$	$E_g(M'')$ (eV)	$\beta(383\text{ K})$
$x = 0.0$	32.299	1.33	1.57	7.17	0.54	0.46	0.43	0.71
$x = 0.1$	29.610	1.51	1.76	1.84	0.51	0.45	0.42	0.45
$x = 0.2$	29.624	2.46	1.77	2.55	0.49	0.43	0.41	0.57
$x = 0.3$	32.301	3.28	1.84	4.97	0.46	0.41	0.40	0.74

Table 2. Rietveld Refined structural parameters, occupancy (N), R_B and R_F of $Zn_{1-x}Ni_xO$ ($x = 0.0, 0.1, 0.2, 0.3$) samples (Space group P63mc: (ZnNi)O).

Sample	$x = 0.0$	$x = 0.1$	$x = 0.2$	$x = 0.3$
$a(\text{\AA})$	3.2486	3.2506	3.2520	3.2502
$b(\text{\AA})$	3.2486	3.2506	3.2520	3.2502
$c(\text{\AA})$	5.2037	5.2070	5.2075	5.2050
$V(\text{\AA}^3)$	47.559	47.649	47.693	47.627
$n(\text{Zn})$	1.0000	0.9000	0.8000	0.7000
$n(\text{Ni})$	0.0000	0.1000	0.2010	0.3000
$n(\text{O})$	1.0000	1.0990	1.0000	1.0990
$R_B(\%)$	2.2800	2.3600	1.4400	1.4200
$R_F(\%)$	1.4600	1.2100	1.0300	1.0400

Table 3. Rietveld Refined structural parameters, occupancy (N), R_B and R_F of $Zn_{1-x}Ni_xO$ ($x = 0.1, 0.2, 0.3$) samples (Space group Fm-3m: NiO)

Sample	$x = 0.1$	$x = 0.2$	$x = 0.3$
$a(\text{\AA})$	4.1983	4.1976	4.1971
$b(\text{\AA})$	4.1983	4.1976	4.1971
$c(\text{\AA})$	4.1983	4.1976	4.1971
$V(\text{\AA}^3)$	73.999	73.962	73.936
$N(\text{Ni})$	1.0000	0.9990	1.0000
$N(\text{O})$	1.0000	1.0000	1.0000
$R_B(\%)$	2.6000	1.7900	3.0100
$R_F(\%)$	1.6900	1.1000	1.6200

Table 4. R-factors (R_p, R_{wp}, R_{exp}), χ^2 and GOF of $Zn_{1-x}Ni_xO$ ($x = 0.0, 0.1, 0.2, 0.3$) samples.

Sample	$x = 0.0$	$x = 0.1$	$x = 0.2$	$x = 0.3$
$R_p(\%)$	7.5400	11.6000	13.5000	15.3000
$R_{wp}(\%)$	8.7300	11.1000	11.5000	11.9000
$R_{exp}(\%)$	4.4600	4.73000	5.36000	5.35000
χ^2	3.8200	5.49000	4.63000	4.97000
GOF	1.9000	2.30000	2.10000	2.20000

4. Conclusions

We have successfully synthesized $Zn_{1-x}Ni_xO$ ($x = 0.0, 0.1, 0.2, 0.3$) nanoparticles by sol-gel technique. The Rietveld refinement of XRD data shows that the samples possess hexagonal structure (space group - P63mc) of ZnO. The low intensity diffraction peaks indicates the presence of NiO, which shows the phase segregation in Ni modified ZnO nanoparticles. Average

crystallite size has been estimated from XRD patterns, which found to increase with increase in Ni content. AC Conductivity increases with the increase in frequency of applied ac field. The hopping frequency of charge carriers increases with the increase in frequency and small polaron hopping conduction mechanism predominates in the studied samples. The dielectric constant and dielectric loss decreases as the frequency of applied ac field increases. The frequency dependent dielectric behavior can be explained on the basis of Koop's theory based on Maxwell-Wagner two layer model. The parameters ϵ' , $\tan\delta$ and ac conductivity increase with increase in temperature due to the increase in drift mobility of the thermally activated charge carriers. The parameters (ϵ' , $\tan\delta$ and ac conductivity) are found to increase with increase in Ni concentration. It may be due to increase in grain size with Ni doping in ZnO. Nearly similar values of activation energy for dc conduction and for conductivity relaxation suggest that the mechanism of electrical conduction and dielectric relaxation are identical. The value of the stretched exponent parameter $\beta < 1$ reveals the presence of non-Debye type of relaxation in the present samples.

Acknowledgment

Authors are thankful to UGC, New Delhi and DST (FIST), New Delhi for financial assistance in the form of grants. One of the authors (Sarita Sharma) is thankful to UGC New Delhi for providing Junior Research Fellowship.

Competing Interests

The authors declare that they have no competing interests.

Authors' Contributions

All the authors contributed equally and significantly in writing this article. All the authors read and approved the final manuscript.

References

- [1] U. Ozgur, Ya.I. Alivov, C. Liu, A. Teke, M.A. Reshchikov, S. Dogan, V. Avrutin, S.J. Cho and H. Morkoc, *J. Appl. Phys.* 98 (2005), 041301.
- [2] A.A. Baladin and K.I. Wang, *Handbook of Semiconductors Nanostructures and Nanodevices*, American Scientific Publisher, Los Angeles (2006).
- [3] T. Gordon, M. Kopel, J. Grinblat, E. Banin and S. Margel, *Mater. Chem.* 22 (2012), 3614–3623.
- [4] F. Ruske, M. Roczen, K. Lee, M. Wimmer, S. Gall, J. Hupkes, D. Hruski and B. Rech, *J. Appl. Phys.* 107 (1) (2010), 013708.
- [5] S. Maniv and A. Zangvil, *J. Appl. Phys.* 49 (1978), 2787.
- [6] E. Fortunato, P.M.C. Barquinha, A. Pimentel, A.M.F. Goncalves, A.J.S. Marques, L.M.N. Pereira and R.F.P. Martins, *Adv. Mat.* 17 (2005), 590.
- [7] T. Dietl, H. Ohno, F. Matsukura, J. Cibert and D. Ferrand, *Science* 287 (2000), 1019.
- [8] H. Ohno, H. Munekata, T. Penney, S. VonMolnar and L.L. Chang, *Phys. Rev. Lett.* 68 (1992), 2264–2667.

- [9] J.H. Zheng, J.L. Song, X.J. Li, Q. Jiang and J.S. Tian, *Cryst. Res. Technol.* 46 (2011), 1143–1148.
- [10] R. Slama, F. Ghribi, A. Houas, C. Barthou and L.E. Mir, *Int. J. of Nanoelectronics and Materials* 3 (2013), 133–142.
- [11] M. Nirmala and A. Anukaliani, *Photonics. Letters of Poland* 2 (2010), 189–191.
- [12] R. Chander, *J. Optoelectron. Adv. Mater.* 13 (2011), 409–411.
- [13] R. Elilarassi and G. Chandrasekaran, *Am. J. Mater. Sci.* 2 (2012), 46–50.
- [14] M. El-Hilo, A.A. Dakhel and A.Y. Ali-Mohamed, *J. Magn. Magn. Mater.* 321 (2009), 2279–2283.
- [15] R. Elilarassi and G. Chandrasekaran, *Mater. Chem. Phys.* 123 (2010), 450–455.
- [16] T. Harbi, *J. Alloy. Compd.* 509 (2011), 387–390.
- [17] S. Udayakmar, V. Renuga and K. Kavitha K, *Int. J. Recent Sci. Res.* 3 (2012), 118–122.
- [18] L. Lutterotti, P. Scardi and P. Maistrelli, *J. Appl. Crystallogr.* 25 (1992), 459–462.
- [19] H.M. Rietveld, *Acta Crystallogr.* 22 (1967), 151–152.
- [20] R.A. Young, *Introduction to the Rietveld Method*, Oxford University Press, Oxford, pp. 1–38 (1993).
- [21] E.J. Mittemeijer and P. Scardi, *Diffraction Analysis of the Microstructure of Materials*, Springer, Germany (2004).
- [22] G.J. Hung, J.B. Wang, X.L. Zhong, G.C. Zhou and H.L. Yan, *J. Mater. Sci.* 42 (2007), 6464–6468.
- [23] W. Li and R.W. Schwartz, *Appl. Phys. Lett.* 89 (2006), 242906.
- [24] B. Gokul, P. Matheswaran, K.M. Abhirami and R. Sathyomoorthy, *J. Non-Crys. Solids* 363 (2013), 161–166.
- [25] F. Barsoukov and J.R. Macdonald, *Impedance Spectroscopy Theory Experiment and Applications*, Wiley-Interscience Press, New York, 2005.
- [26] R. Punia, R.S. Kundu, S. Murugavel and N. Kishore, *J. Appl. Phys.* 112 (2012), 113716.
- [27] R. Punia, R.S. Kundu, M. Dult, S. Murugavel and N. Kishore, *J. Appl. Phys.* 112 (2012), 083701.
- [28] L. Zhang, *Appl. Phys. Lett.* 87 (2005), 022907.
- [29] M.A. Ahmed, E. Ateia and S.I. El-Dek, *J. Matter. Lett.* 57 (2003), 4256.
- [30] M.A. Ahmed and M.A. El Hiti, *J. Chem. Phys.* 23 (1995), 1883.
- [31] M. Dult, R.S. Kundu, S. Murugavel, R. Punia and N. Kishore, *Phys. B* 452 (2014), 102–107.
- [32] Y.S. Wang, P.J. Thomas and P.O. Brien, *J. Phys. Chem. B* 110 (2006), 21412.
- [33] D.P. Almond, G.K. Duncen and A.R. West, *Solid State Ionics* 8 (1983), 159.
- [34] K.W. Wagner, *Am. J. Phys.* 40 (1973)317.
- [35] B. Jaing, J.L. Peng, L.A. Bushil and W.L. Zhong, *J. Appl. Phys.* 87 (7) (2000), 3462.
- [36] M. Mei, Z. Lide and W. Guozheng, *Nanostruct. Mater.* 6 (1995).
- [37] B.P. Das, P.K. Mahapatra and R.N.P. Choudhary, *J. Mater. Sci.: Materials in Electronics* 15 (2004), 107–114.
- [38] R.G. Kharabe, R.S. Devan, C.M. Kanamadi and B.K. Chougule, *Smart. Struct.* 15 (2006), N36–N39.
- [39] R. Vaish and K.B.R. Varma, *J. Appl. Phys.* 106 (2009), 114109.
- [40] K. Majhi, K.B.R. Varma and K.J. Rao, *J. Appl. Phys.* 106 (2009), 084106.

- [41] P. Sharma, D.K. Kanchan, M. Pant and K. Padamasree, *Indian Journal of Pure and Applied Physics* 48 (2010), 39–46.
- [42] R. Bergman, *J. Appl. Phys.* 88 (2000), 1356.
- [43] N. Ponpandian and A. Narayanasamy, *J. Appl. Phys.* 92 (2002), 2770–2778.
- [44] Z. Li and H.Q. Fan, *J. Appl. Phys.* 106 (2009), 054102.